Airborne lidar measurements of wave energy dissipation in a coral reef lagoon system

Zhi-Cheng Huang,[1,2] Benjamin D. Reineman,[1] Luc Lenain,[1] W. Kendall Melville,[1] and Jason H. Middleton[3]

Received 6 April 2011; revised 14 November 2011; accepted 3 January 2012; published 10 March 2012.

[1] Quantification of the turbulent kinetic energy dissipation rate in the water column, ε, is very important for assessing nutrient uptake rates of corals and therefore the health of coral reef lagoon systems. However, the availability of such data is limited. Recently, at Lady Elliot Island (LEI), Australia, we showed that there was a strong correlation between in situ measurements of surface-wave energy dissipation and ε. Previously, Reineman et al. (2009), we showed that a small airborne scanning lidar system could measure the surface wavefield remotely. Here we present measurements demonstrating the use of the same airborne lidar to remotely measure surface wave energy fluxes and dissipation and thereby estimate ε in the LEI reef-lagoon system. The wave energy flux and wave dissipation rate across the fore reef and into the lagoon are determined from the airborne measurements of the wavefield. Using these techniques, observed spatial profiles of energy flux and wave energy dissipation rates over the LEI reef-lagoon system are presented. The results show that the high lidar backscatter intensity and point density coming from the high reflectivity of the foam from depth-limited breaking waves coincides with the high wave-energy dissipation rates. Good correlations between the airborne measurements and in situ observations demonstrate that it is feasible to apply airborne lidar systems for large-scale, long-term studies in monitoring important physical processes in coral reef environments. When added to other airborne techniques, the opportunities for efficient monitoring of large reef systems may be expanded significantly.

Citation: Huang, Z.-C., B. D. Reineman, L. Lenain, W. K. Melville, and J. H. Middleton (2012), Airborne lidar measurements of wave energy dissipation in a coral reef lagoon system, *J. Geophys. Res.*, *117*, C03016, doi:10.1029/2011JC007203.

1. Introduction

[2] Coral reefs are prominent features of shallow water in tropical and subtropical nearshore regions. The geomorphology of coral reefs creates a hydrodynamic environment distinct from that of sandy sloping beaches. The hydrodynamics of coral reefs are influenced by the dramatic transition from relatively deep to shallow water and the rough bottom surface generated by reef organisms [*Monismith*, 2007]. Between the ocean and the shoreline, the geomorphology of a typical fringing reef-lagoon system is composed of a steep fore reef, a gentle reef rim (crest), reef flat and a lagoon.

[3] In recent decades, laboratory and field studies have focused on wave transformation and attenuation of wave energy in the steep transition zone between the fore reef and the outer reef flat [e.g., *Young*, 1989; *Gourlay*, 1994; *Hardy and Young*, 1996; *Lugo-Fernández et al.*, 1998]. These studies have shown that significant wave energy loss comes from the occurrence of depth-limited wave breaking at the seaward reef edge. The large decay of energy due to wave breaking results in a spatial gradient of radiation stress [*Longuet-Higgins and Stewart*, 1964] and causes wave setup [*Gourlay*, 1996a, 1996b; *Massel and Gourlay*, 2000; *Jago et al.*, 2007]. The water surface gradient resulting from the wave setup drives currents on the reef flats, which have been identified by *Symonds et al.* [1995], *Gourlay and Colleter* [2005] and *Lowe et al.* [2009].

[4] In addition to the dissipation due to wave breaking, bottom friction is another significant contributor to wave energy dissipation over reef flats [*Young*, 1989; *Lowe et al.*, 2005]. The presence of coral forms a rough bottom surface, with drag due to both normal and viscous stresses affecting turbulent shear stresses, which, with current gradients produce turbulent kinetic energy (TKE) that is ultimately dissipated by viscosity [*Tennekes and Lumley*, 1972; *Monismith*, 2007]. Measuring dissipation rates on the reef flats is difficult, but some estimates have been reported by *Nelson* [1996], *Falter et al.* [2004] and *Lowe et al.* [2005].

[1]Scripps Institution of Oceanography, University of California, San Diego, La Jolla, California, USA.
[2]Now at Graduate Institute of Hydrological and Oceanic Sciences, National Central University, Taoyuan, Taiwan.
[3]School of Aviation, University of New South Wales, Sydney, New South Wales, Australia.

0148-0227/12/2011JC007203

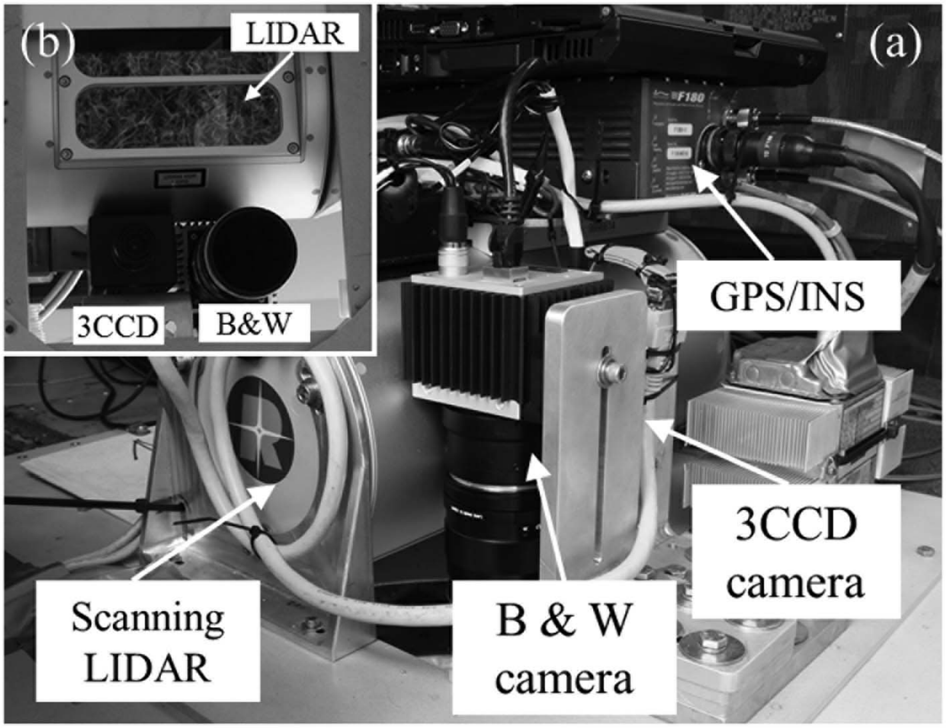

Figure 1. Instrumentation for the airborne lidar measurements. (a) The scanning lidar, GPS/INS, 3CCD camera, and black and white (B & W) camera were mounted in the cabin of the Cessna Caravan aircraft. (b) Also shown is the view upward from below the aircraft.

Huang et al. [2012] quantified the wave dissipation rates over the Lady Elliot Island (LEI) reef lagoon. These studies showed that the decay of wave energy on the reef flat and in the lagoon is related to the frictional dissipation due to the rough bottom surface.

[5] Energy dissipation rates indirectly influence the biogeochemical status of the reef and many coral reef processes including morphological evolution, marine organism distributions and nutrient uptake [*Gourlay*, 1994; *Hearn et al.*, 2001; *Baird et al.*, 2004; *Falter et al.*, 2004; *Reidenbach et al.*, 2009]. As a result, quantification of dissipation rates is important for modeling and monitoring the hydrodynamics and ecology of reef-lagoon systems. It is difficult and expensive to measure dissipation rates in the field, consequently there have been few in situ studies [e.g., *Nelson*, 1996; *Falter et al.*, 2004; *Lowe et al.*, 2005, *Huang et al.*, 2012]. This presents a challenge in monitoring large reef systems, like the Great Barrier Reef, since it is not feasible to conduct in situ monitoring over large areas of the reef. This leads to the need to develop other efficient methods of monitoring energy dissipation rates in large reef-lagoon systems.

[6] *Reineman et al.* [2009] developed a portable and cost-effective airborne lidar system for ocean and coastal applications. With the development of lighter and cheaper commercial lidars and GPS/inertial navigation systems (INS), many scientific and technical problems can be addressed using small aircraft. We have already demonstrated that the TKE dissipation rates in the Lady Elliot Island (LEI) lagoon can be related to the wave dissipation rates, which are determined by measuring the spatial gradients in the wave energy fluxes [*Huang et al.*, 2012]. This motivates the question of whether the spatial gradients in the wavefield, and therefore the wave energy dissipation, and by implication the TKE dissipation in wave-dominated flows, can be measured by airborne lidar. If it can, then large reef systems could be monitored by airborne techniques.

[7] In this paper, we describe the performance and test the feasibility of using the airborne lidar system for observing the wave dissipation rates over the reef-lagoon system around LEI (24.11°S, 152.72°E), located off the southeast coast of Queensland, Australia, in the Great Barrier Reef. In section 2, we present the airborne lidar measurements and review in situ measurements. In section 3, we describe the data analysis methods. The results of the wave energy flux and wave dissipation rate measurements are presented in section 4. The summary and conclusions are given in section 5.

2. Field Measurements

[8] The airborne scanning lidar system developed by *Reineman et al.* [2009] was installed in the cabin of a Cessna Caravan aircraft (Figure 1) to measure the island topography, the lagoon, reef and surrounding wavefield of Lady Elliot Island. A detailed description of the airborne scanning lidar system is given by *Reineman et al.* [2009].

[9] When operating the airborne lidar surveys over LEI, waypoints were programmed into the aircraft navigation system to give parallel tracks spaced 125 m apart over the area of interest, at altitudes of 110 to 130 m, oriented

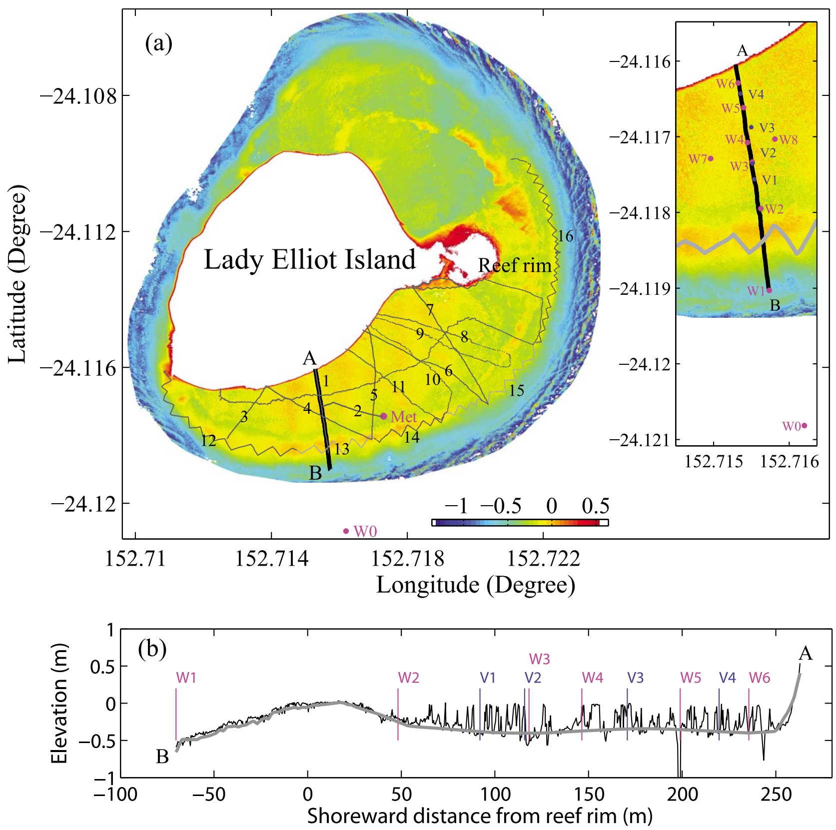

Figure 2. (a) Lady Elliot Island (located off the southeast coast of Queensland, Australia, in the Great Barrier Reef), surrounding wavefield, reef rim and transect of the in situ instrument deployment (A-B). The topographic map was constructed from multiple passes at low tide using an airborne portable scanning laser altimeter system (lidar), described in *Reineman et al.* [2009]. Gray lines with marked numbers are manual bathymetric surveys. (b) Manual bathymetric transect of line A-B (black line), objective-mapping bathymetric transect of line A-B (gray line) at bottom of coral heads, and the locations of the instruments. Wave gauges and ADV locations are shown as W0-W6 and V1-V4, respectively. The elevation is referenced to the mean rim elevation. Wave measurements at W1 and W2 failed.

north-south and east-west to maximize spatial coverage of the island and lagoon.

[10] Concurrent in situ measurements (3–24 April 2008) were conducted to characterize the wavefield, currents and turbulence in the lagoon [*Huang et al.*, 2012]. Figure 2 shows an elevation map of the island, reef rim, reef flat and surrounding wavefield during a spring low tide measured by the airborne scanning lidar system described above. The windward coral reef lagoon is about 200 m wide between the reef rim and the beach. The line A-B oriented in a cross reef direction was selected for in situ measurements of the wave energy dissipation rate over the coral reef and lagoon, and TKE dissipation rates in the lagoon. One pressure-temperature (PT) sensor was deployed on the fore reef while two PT sensors and six ultrasonic wave gauge systems were distributed in the lagoon to measure the wave energy and wave dissipation rates across the fore reef into the lagoon. Three-component near-bottom flow velocities were measured by four acoustic Doppler velocimeters (ADVs) in the lagoon. Detailed manual GPS bathymetric surveys were conducted over the windward lagoon. The measured standard deviation of the bottom bathymetry, σ_b, is approximately a constant value of 0.14 m for the whole windward lagoon. It was shown that a single length scale of bottom roughness can be applied to estimate the frictional dissipation in the lagoon [*Huang et al.*, 2012]. Detailed descriptions of the in situ instrumentation are given by *Huang et al.* [2012].

[11] The wind, wave and tide conditions from the in situ measurements during the airborne flight surveys are presented in Figure 3. The wind was steady and strong (U_{10} = 7–11 m s^{-1}, θ_{wind} = 140 – 170°) for year days 97–101 and 107–114, and was weak and variable (U_{10} = 2–7 m s^{-1}, θ_{wind} = 70–190°) for year days 102–106. The significant wave heights, defined as $Hs = 4[\int S(f)df]^{1/2}$, where S is the spectral density of the surface displacement and f is the frequency in Hz, at site W0 (Hs_0, on the fore reef in the ocean) increased with the wind speed U_{10} [*Huang et al.*, 2012]. Hs_0 was in the range 1.5–3 m and 0.7–1.2 m for the stronger and weaker wind fields, respectively. The peak wave period, defined as $T_{p0} = [\int S^5(f)df]/\int fS^5(f)df]$, was about 5 s and 10 s for days corresponding to the strong and weak wind fields, respectively. The recorded tide shows that the differences between the elevations outside and inside the lagoon reach up to approximately 0.6 m at low tide. The

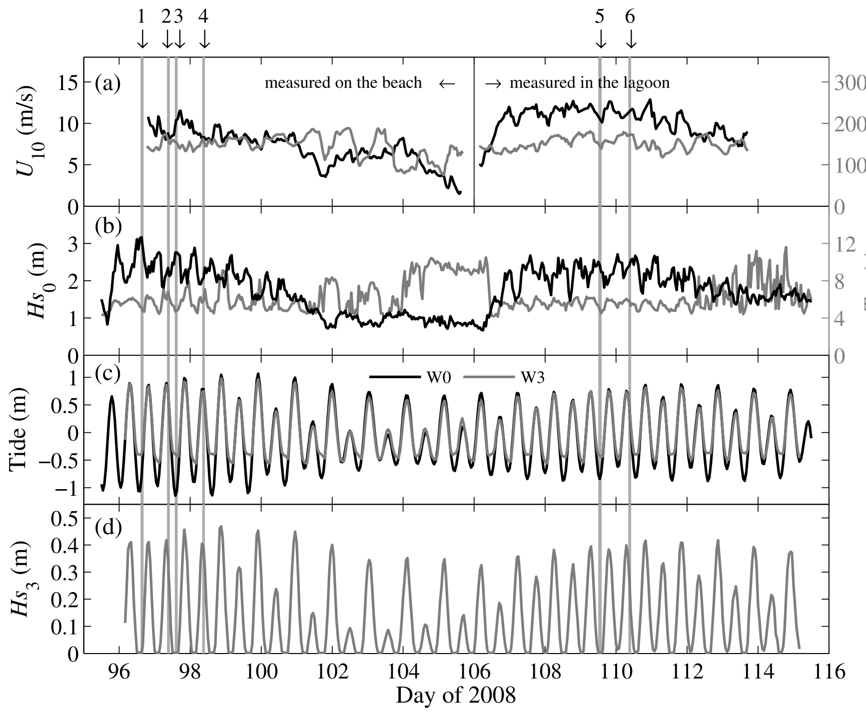

Figure 3. Time series of wind, wave and tides during the experiment with the flights marked by gray lines. (a) Wind speed U_{10} and wind direction θ_{wind} (from). (b) Significant wave height Hs_0 and weighted peak wave period of surface displacement at the ocean (site W0). (c) Tidal elevation (represented as a deviation from the mean) in the ocean (W0, black line) and in the lagoon (W3, dark gray line). (d) Significant wave height in the lagoon (site W3). The numbers 1–6 at the top of the figure indicate the times of the six lidar flights. Detailed wind, wave, tide, and flight conditions for the six flight surveys are given in Table 1.

lagoon is isolated from the ocean during the spring low tides because the elevation of the reef rim is higher than the sea level in the ocean. Airborne measurements of the wave dissipation rate were conducted from a total of 49 flight passes over the central windward lagoon during three high-tide and three low-tide surveys. Each flight includes 7–10 passes over the lagoon, and 30 transects of the surface elevation in each pass were analyzed. This results in a total of 210–300 profiles being used to determine the wave energy flux for a particular flight. Detailed flight timestamps, number of flight passes, wind, wave, and tide conditions of the six flight surveys are summarized in Table 1.

[12] A bathymetric map over the windward LEI reef platform is needed to give the water depth for computing wave group velocity, wave energy fluxes and wave dissipation rates due to the areal coverage of the airborne measurements. Bottom elevations from the manual GPS surveys in the lagoon were extracted from all the surveyed lines by identifying local minimum elevations in bathymetric profiles as demonstrated for defining canopy elements by *Huang et al.* [2012]. The bottom elevation data were then interpolated on a regular grid over the central lagoon with a 15 m × 15 m resolution using an objective mapping algorithm [*Bretherton et al.*, 1976]. Based on the density of the surveyed lines, the decorrelation length scale of the objective mapping was set at 50 m. This elevation map was combined with the high-resolution airborne lidar bathymetric data of the exposed bottom and coral at low tide, especially the exposed reef rim and reef flat in Figure 2. They were then interpolated on a 2 m × 2 m grid in the N × E directions using a bilinear interpolation algorithm to determine the bathymetric map over the lagoon. A comparison of the objectively mapped interpolated bathymetric data with the manual GPS data is shown in Figure 2b.

[13] Three other sources of bathymetric data outside the reef rim were included to determine the water depth around the whole LEI reef platform. The first is a side-scan sonar survey (Klein 5000 towed light weight sonar) that was undertaken by the Australian Hydrographic Office in 2000; the second, provided by one of the authors (JHM), is a shipboard ADCP survey from 2001; the third, provided by R. McCabe (personal communication, 2009), is a shipboard ADCP survey from 2008. All the bathymetric data were gridded and linearly interpolated on a regular grid with a spacing of 2 m × 1 m in the N × E directions to obtain the bottom topographic map surrounding the LEI reef platform. In general, except for the reef platform in the SW direction outside the reef rim, the topography of the reef platform is radially distributed with decreasing contour levels that are almost parallel to the reef rim.

3. Data Analysis

[14] The received lidar backscatter intensity was averaged in the cross-flight (cross-swath) direction to determine the along-track profile of the cross-swath averaged backscatter

Table 1. Wind, Wave, Tide, and Flight Conditions of Airborne Lidar Surveys[a]

Flight Number	Start Time (Year Day in 2008)	Duration (min)	Total Flight Passes Over the Central Windward Lagoon	Number of Transects, N, Being Analyzed	Tidal Range Referenced to the Mean (m)	Wind Speed U_{10} (m/s)	Wind Direction (From) (deg)	Hs_0 Ocean (m)	Tp_0 Ocean (s)	Hs_3 Lagoon (m)	h_3 (m)
1	96.630	45	7	210	−0.702 to −0.412	–	–	2.918–3.131	4.80–5.09	0.006–0.027	0.472–0.539
2	97.375	45	8	240	0.538–0.825	8.35–8.78	154–161	2.178–2.340	6.32–6.82	0.259–0.350	1.338–1.591
3	97.592	42	10	300	−1.046 to −0.985	10.04–10.42	152–155	2.757–2.757	4.72–4.78	0.002	0.441–0.459
4	98.365	32	7	210	0.790–0.868	8.28–8.33	157–162	2.059–2.157	5.80–6.20	0.368–0.396	1.552–1.609
5	109.529	60	9	270	−0.688 to −0.759	10.36–10.65	142–147	2.290–2.447	4.62–5.01	0.003	0.425–0.444
6	110.371	44	8	240	0.561–0.293	11.39–11.52	172–174	2.402–2.496	5.51–5.87	0.194–0.280	1.121–1.353

[a]Note that the flight numbers 1, 3, and 5 are at low tides, while flight numbers 2, 4, and 6 are close to high tides.

intensity, I, in arbitrary units The normalized cross-flight point density, PD, is defined as the number of received points divided by the total number of the scanning points for each cross-flight scanning line, i.e., 0 and 1 means no or all scanning points returned in each scanning line, respectively. Sample airborne lidar data showing cross-swath averaged backscatter intensity, normalized cross-flight point density, and sea surface displacement for a high-tide survey are presented in Figure 4. Clearly, a larger swath width results from the high backscatter intensity and point density region seaward of the rim. The lidar gives higher backscatter intensity and point density over the land and in the surf zone of depth-induced wave breaking than over the ocean. The backscatter intensity and the point density depend on the surface reflectivity and target angles relative to the laser pulses. The ocean surface is significantly less reflective than the structures over the land, so there are fewer returns and a lower point density over the ocean [*Reineman et al.*, 2009].

[15] Georeferenced data points of the sea-surface displacement were interpolated using a Kriging method [*Stein*, 1999] and regularly gridded with spatial resolutions of 2 m × 1 m in the N × E directions. Thirty straight transects of the measured sea surface in each pass, or swath, were then transformed into the along-track coordinate with a constant spacing of 2 m in the along-track direction using a bilinear interpolation.

[16] Subareas of the gridded sea surface elevation with a size of 200 m (north) × 200 m (east) (windows A and C in Figure 5a) and a size of 100 m (north) × 200 m (east) (window B in Figure 5a) were interpolated with a spatial resolution of 1 m × 1 m using a bilinear interpolation, and were then padded with zeros to a 512 × 512 matrix of nodes. The zero-padded subareas of sea surface elevation were analyzed by two dimensional fast-Fourier transforms (FFT) with mean removal, linear detrending, and correction of Doppler shift to determine the directional wavenumber spectra, $S(k, \theta)$, as demonstrated in Figure 5d. Assuming a linear dispersion relationship,

$$\omega^2 = gk \tanh kh, \tag{1}$$

where ω is the radian frequency, g the gravitational acceleration, $k = (k_x^2 + k_y^2)^{\frac{1}{2}}$ the wavenumber, and h the water depth, the change of the wavenumber component due to the Doppler effect in the along-track or x-direction, δk_x, was corrected iteratively by

$$\delta k_x = -\frac{\omega}{\nu_a} \tag{2}$$

and assuming a constant water depth h and aircraft velocity ν_a over each area [cf. *Walsh et al.*, 1985] . Starting with the measured k_x, and using equation (1), the correction is computed, then the corrected k and ω are used in equation (2) for the next correction. Typically three to four iterations are needed for each k_x.

[17] Figure 6 shows the measured sea surface topography from five passes during a high-tide flight on 19 April (flight 6) in Table 1. The superimposed wave directions were determined from the computed directional wavenumber spectra by defining the wave direction of the energy of the

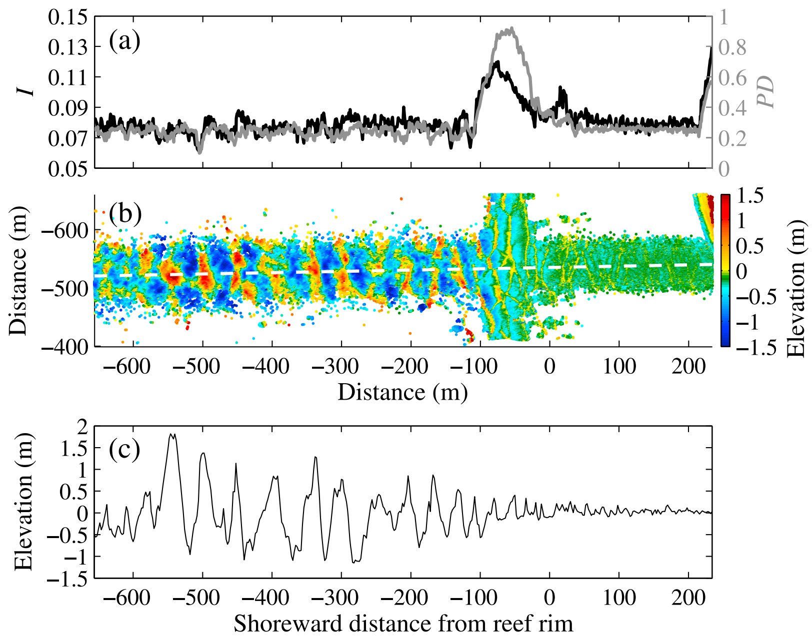

Figure 4. Sample airborne lidar data of backscatter intensity, point density, and sea surface elevation map from a flight at high tide. (a) Spatial profiles of the cross-swath averaged backscatter intensity, I (in arbitrary units), and normalized cross-flight point density, *PD*. *PD* is the fraction of return points in each scanning line, i.e., 0 and 1 means no or all scanning points return, respectively. (b) Sea surface displacement map from one pass. Waves are propagating from left to right, breaking in front of the rim, which shows a larger swath width caused by the higher reflectivity of foam from breaking waves, and continuing through the lagoon toward the island. (c) Profile of sea surface elevation of the transect marked by the white dashed line in Figure 4b.

integral over all wavenumber components, using the weighted group velocity

$$\bar{c}_g(k,\theta) = \frac{\iint c_g(k,\theta) S(k,\theta) k dk d\theta}{\iint S(k,\theta) k dk d\theta} \quad (3)$$

that conserves the energy flux [see *Drazen et al.*, 2008]. The results show that the wave direction is nearly uniform with a variation of few degrees for passes close to the location of the in situ measurements, and the variation is less than 20° for the farthest pass. This confirms the in situ observation that the waves propagate almost unidirectionally across the lagoon [*Huang et al.*, 2012]. The reef rim is located by searching the maximum bottom elevations in transects of the topographic map between the fore reef and the island, and the origin is defined at the outer edge of the reef flat. The position of the reef rim for passes over the central windward lagoon is shown with the solid black line in Figure 6.

[18] Each transect of the sea surface elevation (e.g., Figure 5b) was analyzed by wavelet transform techniques with mean removal and linear detrending to determine the instantaneous dominant wavenumber $k_{p,n}(x)$ of the surface waves from the amplitude-wavenumber spectrum (Figure 5c), where x is the along-track shoreward distance from the rim and the subscript n denotes the n*th* transect of the flight survey, or swath. The wavelet kernel adopted here is the Morlet wavelet, $\varphi(x) = e^{ik_0 x} e^{-x^2/2}$ [*Farge*, 1992; *Emery and Thomson*, 2001], where k_0 is the wavelet's central wavenumber and was set at a commonly adopted value of 6 [*Farge*, 1992]. In the analysis, the boundary values are extended and kept constant to eliminate the boundary effects during the translating process [*Huang et al.*, 2010]. The dominant wavenumber $k_{p,n}$ is defined as the wavenumber of the energy peak in the spectrum. The instantaneous wave frequency, $\omega_n(x)$, was calculated using the linear dispersion relationship, equation (1), where $h_n(x)$ is the local water depth of the nth transect of the flight swath. The water depth was determined from the georeferenced topography with a known tidal elevation. Again, following *Walsh et al.* [1985], the wavenumber was corrected iteratively for Doppler shift due to the relative motion between the wave phase speed and the aircraft velocity (equation (2)). The mean aircraft ground speed was about 30–40 m s^{-1} and 50–60 m s^{-1} for the upwind and downwind passes, respectively. The Doppler shift was corrected using the varying aircraft speed in each pass. All transects of the flight passes were analyzed by the above procedure to determine profiles of the instantaneous wavenumber spectra, as in Figure 5c, and wave frequency.

[19] Flights 1–6 each contained 7–10 passes over the center of the windward lagoon. Thirty transects of the measured sea surface were analyzed in each pass; therefore, 210–300 (N) transects were used to compute an ensemble-averaged profile. The ensemble averaging of a specific quantity q (wavenumber, wave energy, wave group velocity, energy flux) over N profiles is defined as

$$q(x) = \langle q_n \rangle = \frac{1}{N} \sum_{n=1}^{N} q_n(x,t), \quad (4)$$

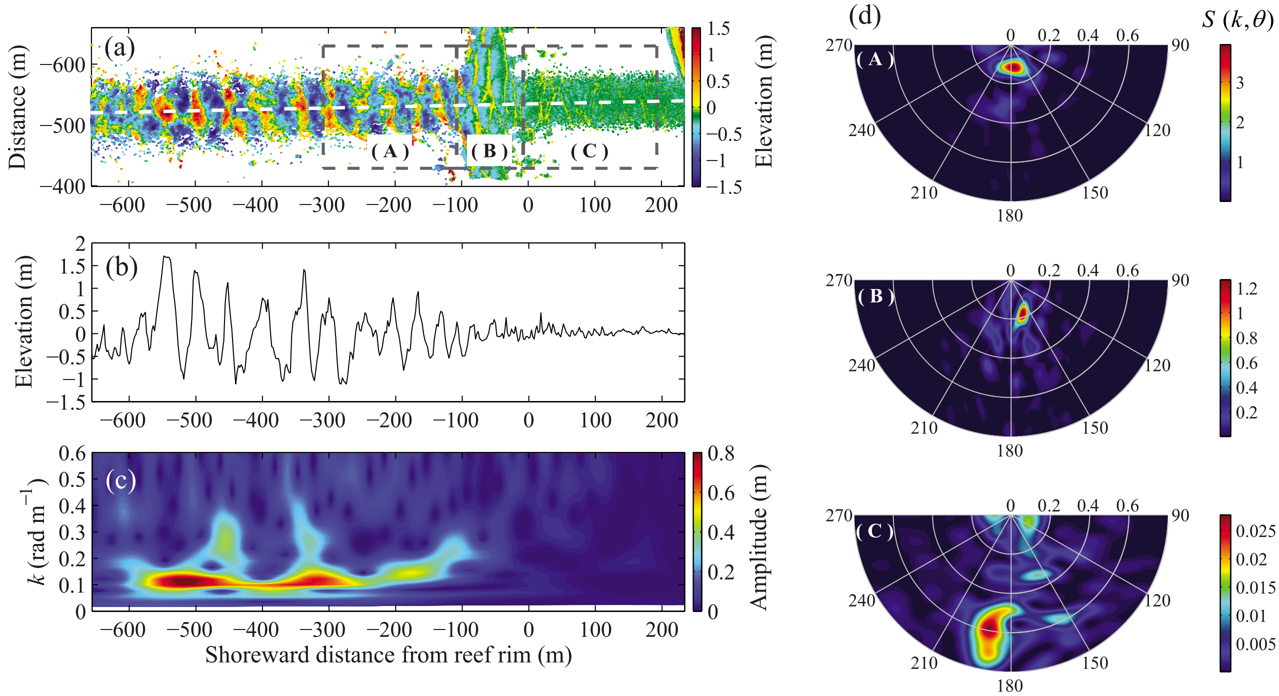

Figure 5. Illustration of the lidar data analysis techniques. (a) Sample sea surface displacement map from one pass of a high-tide survey. (b) Profile of sea surface displacement of the transect marked by the white dashed line in Figure 5a. (c) Amplitude-wave number contour map obtained by analyzing the transect of sea surface using 1D wavelet transform technique with a Doppler shift correction to account for the aircraft velocity over the ground. (d) Directional wavenumber spectra, $S(k, \theta)$ (m^4 rad^{-3}), obtained by analyzing the subareas of the sea surface map marked by the dark gray dashed windows (A, B, and C) in Figure 5a using 2D fast-Fourier transform with Doppler-shift correction. Note the different color scales for each spectrum.

where x is the along-track shoreward distance from the rim, the subscript n denotes the nth transect of the flight surveys, the angle brackets represent an ensemble-averaging over the N profiles. Note that if the wavefields were stationary, the ensemble averaging is equivalent to time averaging. In averaging the airborne measurements, the mean value converges to within acceptable errors with a finite number of transects. As with almost all geophysical variables, it is a matter of compromise between having a short enough data window for stationary conditions while having a large enough ensemble to achieve reasonable convergence of the statistics. It might be better to perform the ensemble averaging from multiple flight passes over the same track, but ensemble averaging in the present study was performed for flight passes spaced over the LEI windward lagoon due to similar features of bottom roughness and wave direction in the lagoon. Notice that the along-track coordinates were shifted into a coordinate system relative to the shoreward distance from the rim because the depth-limited wave breaking and the wave attenuation in the lagoon are correlated with the water depth over the rim and shoreward distance from the rim [*Huang et al.*, 2012].

[20] For high-tide conditions, waves were filtered by the depth-limited wave breaking, with some transmission into the lagoon. Figure 7 illustrates a profile of the ensemble-averaged peak wavenumber and its standard deviation from the averaging for a high-tide survey, shown with the mean water depth and lidar cross-swath averaged backscatter intensity. It shows that the average peak wavenumber starts to increase in the fore reef (approximately $-300 < x < -100$ m) due to wave shoaling, continues increasing across the surf zone (approximately $-100 < x < 50$ m, the region of high backscatter intensity in Figure 7a), and decreases gradually in the lagoon (approximately $50 < x < 240$ m). In the averaging, the standard deviation represents the range of the instantaneous dominant wavenumbers. The standard deviation does not increase in the fore reef, but starts to increase in the surf zone, and remains nearly constant in the lagoon. The increase in range of the dominant wavenumber is similar to the broadening of the two-dimensional FFT wavenumber spectrum shown in Figure 5, and is similar to the broadening of typical frequency spectra over reef flats observed in other studies [e.g., *Hardy and Young*, 1996]. Similar distributions of the dominant wavenumber were observed in other high-tide airborne surveys. The profile of the ensemble-averaged dominant wavenumber for a low-tide survey is given in Figure 8. The distribution of the dominant wavenumber on the fore reef outside the surf zone for low-tide surveys (approximately $x < -200$ m) is similar to that in high tides; however, the dominant wavenumber inside the surf zone at low tide (approximately $-150 < x < -50$ m) is distinct from that at high tide. The average dominant wavenumber continues increasing across the surf zone at high tide. In contrast, the average dominant

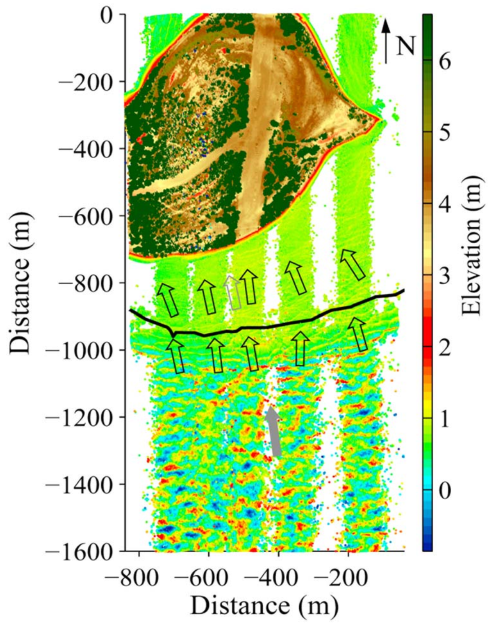

Figure 6. Sea surface displacement of high-tide lidar data for five passes on 19 April 2008 (flight 6 in Table 1). The wider swath region indicates the surf zone of the depth-limited wave breaking. The hollow black arrows are weighted mean wave directions determined from the computed directional wavenumber spectra weighting the group velocity by the spectral wave energy density to define the mean energy flux. The hollow gray arrow is the wave direction (from 168°) determined by the in situ wave gauge array. The filled gray arrow is the wind direction (from 172°). The solid line is the defined reef rim position for all flight passes over the central windward lagoon.

wavenumber decreases toward the shoreline in front of the rim at low tide.

[21] With aircraft groundspeeds in the range of 30–60 m s^{-1}, much greater than the phase speed or group velocity of the surface waves, the wave data in Figures 4, 7 and 8, are, to leading order, spatial data. To compare with the much more common wave time series data from point measurements, it is useful to consider how much spatial data there is relative to the more common time series data. Surface wave data at a point are commonly measured for 20 min records, and the transformation from spatial to temporal data can be obtained using a characteristic group velocity of the surface waves. For example, using the data from Figure 7 for the 8 passes of flight 6, we will consider the spatiotemporal transformation for the waves offshore before a significant shoaling begins, say for $-1000 < x < -500$ m, and in the lagoon, a fetch of approximately 200 m. Offshore, the dominant wavenumber is approximately 0.15 rad m^{-1} for a wavelength of 42 m; so 8 passes of 500 m represents 96 wavelengths. Twenty minutes at the group velocity of those deep-water waves would cover 115 wavelengths, or 20% more. This is the calculation for one transect in each pass or swath. But if the waves are not completely correlated across the swath, and if as little as two independent transects could be used per swath, then the airborne coverage would double to being equivalent to 33 min of data. Doing the same calculation in the lagoon where the dominant wavelength in Figure 7 is approximately 18 m, and the depth approximately 1.4 m, then 8 passes of 200 m represents 89 wavelengths. Twenty minutes at the group velocity of those waves represents 247 wavelengths. There is significantly more decorrelation of the waves across the approximately 100 m swath in the lagoon (Figure 4). Consistent with the 50 m decorrelation scale used to map the variability of the bathymetry in the lagoon, we expect to be able to use at least 3 independent transects in one swath of 100 m width, which would give $3 \times 89 = 267$ wavelengths; being equivalent to 22 min worth of data. Thus the spatial coverage of the aircraft data is of the same order of magnitude as, or comparable to, standard time series data.

4. Observation of the Wave Dissipation Rate

[22] By equipartition, the average total wave energy density per unit area, $E(x)$, is estimated as twice the potential energy density

$$E = \langle E_n \rangle = \left\langle \rho g (\eta_n - \bar{\eta}_n)^2 \right\rangle, \tag{5}$$

where ρ is the water density, $\eta(x)$ is the surface elevation. For the lidar data, the overbar denotes a spatial average and the angle brackets an ensemble average. For the in situ time series data both symbols in equation (5) represent time-averaging. Spatial profiles of the wave energy density were computed using equation (5) with mean removal and linear detrending.

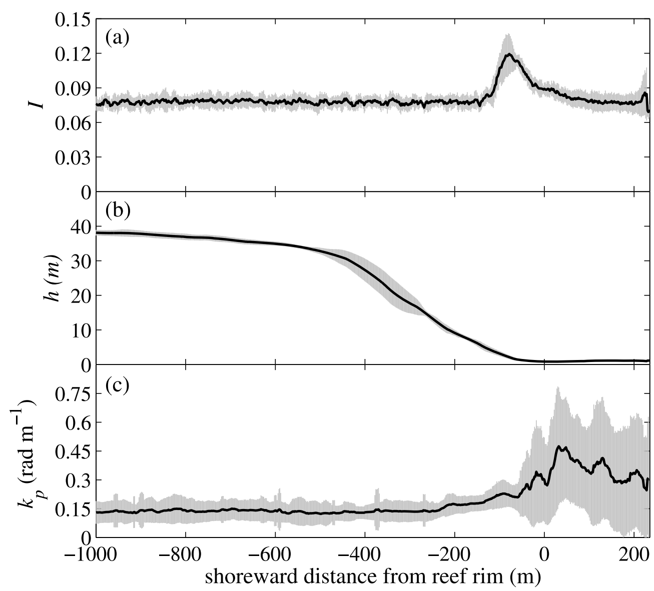

Figure 7. Example of ensemble-averaged profiles of backscatter intensity, water depth, and wavenumber for high-tide flight 6 on 19 April 2008. Gray vertical lines show the standard deviation from the average. (a) Average profiles of the cross-swath backscatter intensity, $I = \langle I_n \rangle$ (arbitrary units). (b) Averaged water depth, $h = \langle h_n \rangle$. (c) Averaged dominant wavenumber, $k_p = \langle k_{p,n} \rangle$. The range of the dominant wavenumber starts to broaden inside the surf zone (high backscatter intensity region) and through the lagoon.

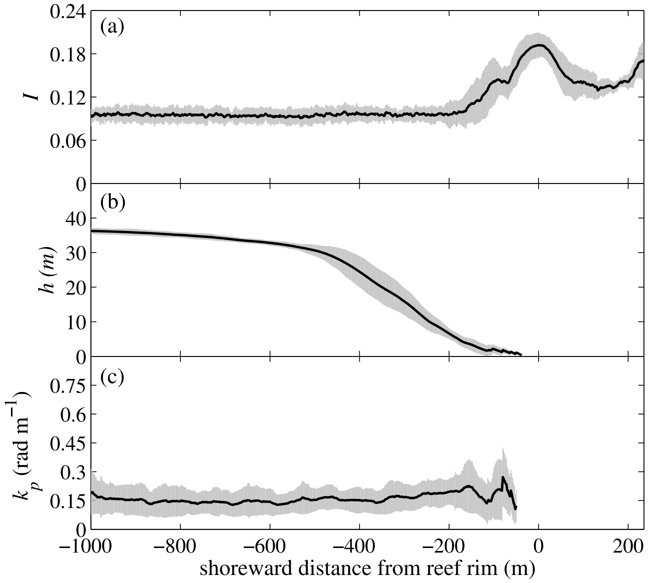

Figure 8. Example of ensemble-averaged profiles of lidar backscatter intensity, water depth, and wavenumber at low-tide for Flight 3 on 6 April, 2008. Vertical gray lines show the standard deviations from the average. (a) Average profiles of the cross-swath backscatter intensity (arbitrary units), $I = \langle I_n \rangle$. Backscatter intensity inside the lagoon is high at low tide due to the exposed reef. (b) Averaged water depth, $h = \langle h_n \rangle$. (c) Averaged dominant wavenumber, $k_p = \langle k_{p,n} \rangle$. Note that for the low-tide flights, the computation of dominant wavenumber is only performed in the ocean due to the isolation of the lagoon at low tide.

[23] Since only 7–10 passes were conducted for each flight, the ensemble-averaged results of the wave energy density and wave energy flux oscillated in the along-track direction. The relatively small number of passes means few samples are used for averaging in the time domain; however, assuming a slow variation in the time-space transformation, bin averaging in the spatial domain smoothes the data. The ensemble-averaged profiles, therefore, are running-bin averaged to reduce the uncertainties of the averaging in the time domain. A varying window size that is related to the local dominant wavelength is chosen for the bin averaging. The average dominant wavelength, λ, obtained from inverting profiles of the ensemble-averaged dominant wavenumber for each flight, was adopted for scaling the bin-averaging window as shown in Figure 9a. Because the wave energy oscillated wave by wave and was also modulated by wave groups, the bin-averaging window size should be chosen with a length larger than one wavelength, or even larger than a wave group length. The wavelet-transformed amplitude-wavenumber spectra (Figure 5c) show that the wave group length is about 200–250 m in the ocean. In addition, the window size in front of the rim should not exceed the surf zone width (about 100–150 m) to avoid the large gradient in the surf zone being smoothed out. Combining these limitations, an appropriate window size would be in the range of 1–4 times the average dominant wavelength since the average dominant wavelength is about 20–30 m in front of the rim. A test of the bin-averaged wave energy profile with window sizes of 3–4λ is given in Figure 9b. The variation of the bin-averaged results with different window sizes is small when applying a window larger than 2λ. The variation increases for the results in the surf zone when the window is larger than 4λ. This may suggests a window size of 3λ would be the best compromise. The variation and uncertainty using different window size (2–4λ) is shown for all the following results.

[24] The comparison of the wave energy density measured by the airborne lidar and by the in situ measurements [*Huang et al.*, 2012] is given in Figure 10a. Satisfactory agreement of the results between the two independent methods is obtained for high-tide surveys. The airborne lidar data for the lagoon (for data less than 200 J m^{-2}) show higher estimates than those of the in situ measurements. Note that a very small uncertainty of the lidar measurements of the sea surface displacement leads to a larger value of wave energy density. For example, an uncertainty of 0.03 m leads to an error of 9 J m^{-2} in wave energy density. The mean value of the standard deviation of airborne lidar measured energy density being smoothed by different window sizes is 3.68 J m^{-2} in the lagoon. In addition, a larger discrepancy exists at site W0 for low-tide surveys. Since the pressure-temperature (PT) sensor at site W0 deployed in front of the rim was very close to the surf zone at low tide, the PT sensor may over-estimate the variance of the surface elevation when linear wave theory is used to convert the pressure data to surface elevation.

[25] The spectrally averaged wave group velocity $C_{gw}(x)$ is calculated by weighting the group velocity by the square of the wave amplitude using linear wave theory [cf. *Drazen et al.*, 2008]

$$C_{gw}(x) = \frac{\sum C_{g,n}(k) a_n^2(x;k)}{\sum a_n^2(x;k)}, \tag{6}$$

$$C_{g,n} = \frac{\omega_n^2 + g k_n h_n(x)[1 - \tanh^2(k_n h_n(x))]}{2\omega_n k_n}, \tag{7}$$

where $a_n^2(x;k)$ is the amplitude of the energy in the amplitude-wavenumber spectrum obtained by the wavelet transform

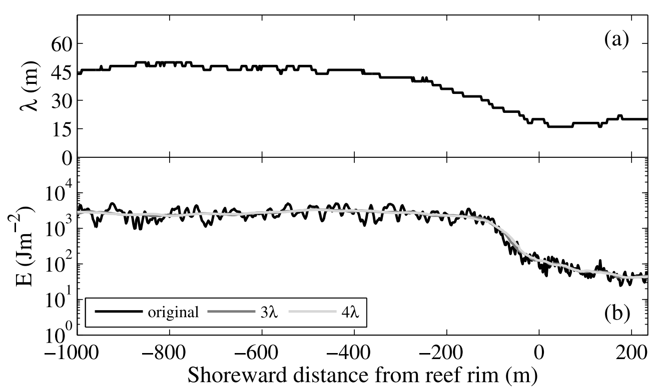

Figure 9. Example from Flight 6 of running-bin averaging with a varying window size related to the local wavelength. (a) Average dominant wavelength, λ, obtained by inverting the ensemble-averaged dominant wavenumber. (b) Original and bin-averaged ensemble-averaged wave energy density profiles with a window size of 3–4λ.

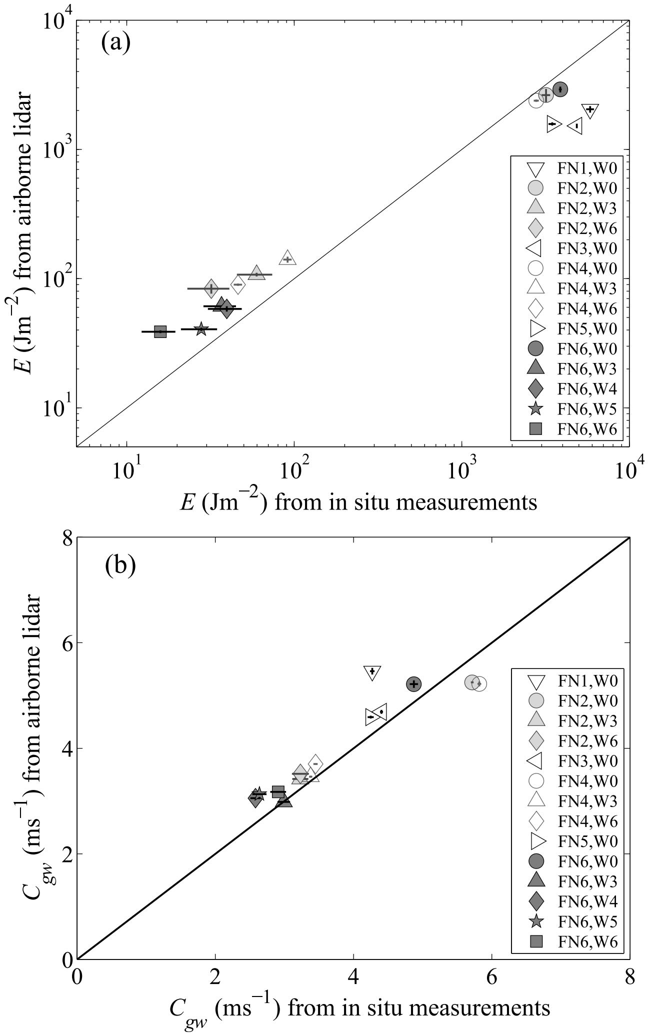

Figure 10. Comparison of (a) the wave energy density and (b) weighted wave group speed, observed by the airborne lidar and by in situ wave gauge measurements, with horizontal bars showing the standard deviation of the in situ measurements during the airborne flight time period and vertical bars showing the standard deviation of the running-bin averaging with a window size of 2–4λ, depending on spatial gradients. Legend shows flight numbers (FN#) and measurement locations (W1-W6) in Figure 1.

(Figure 5c). Spatial profiles of the wave group velocity were computed from equations (6) and (7), and then bin averaged with window sizes of 2–4λ. The comparison of the wave group velocity determined by airborne lidar and by in situ measurements is given in Figure 10b. The mean value of the standard deviation of airborne lidar measured wave group velocity being smoothed by different window sizes is 0.01 m s^{-1} in the lagoon. In general, the two independent methods show good agreement, although a discrepancy exists for the data at site W0 close to the surf zone.

[26] The spectral average energy flux F per unit area is defined as

$$F = \langle F_n \rangle = \langle E_n C_{g,n} \rangle. \tag{8}$$

The wave energy flux was computed using equation (8) and then was bin averaged, and shown with the standard deviation using window sizes in the range 2–4λ. In the absence of other significant wave energy source terms (e.g., wind input) and with the application of the energy balance equation in a control volume, the total wave energy dissipation rate D_{air} for one-dimensional propagation of the waves can be calculated from the measured spatial gradient of the energy flux

$$D_{air} = -\frac{\Delta F}{\Delta x \cdot \cos\theta}, \tag{9}$$

where θ is the angle between the wave propagation direction and the along-track direction, Δx is the distance between two specific points for observing the energy flux along the

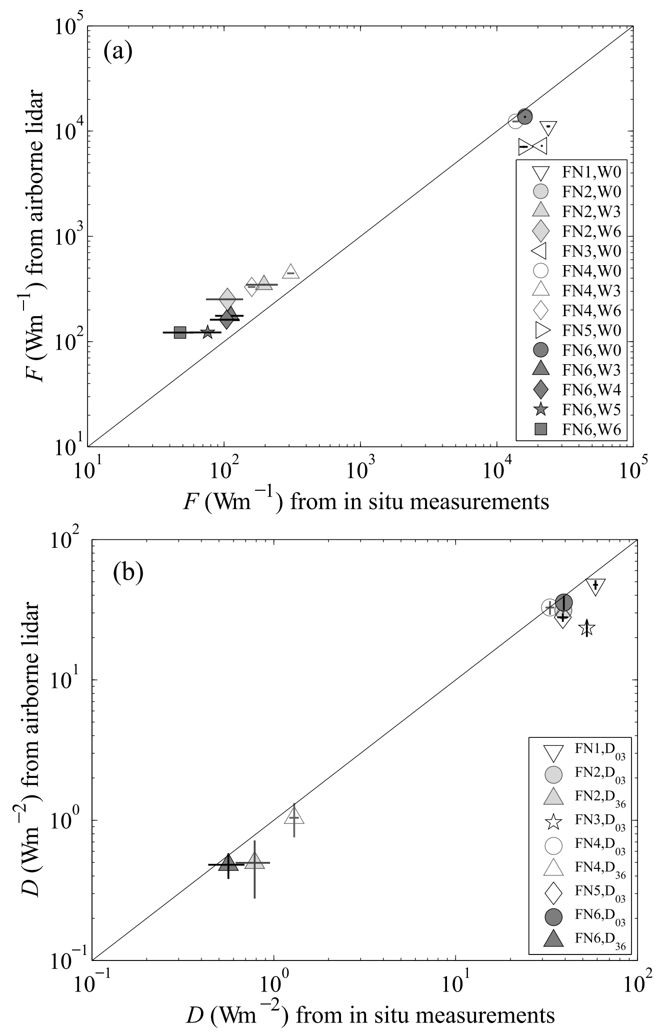

Figure 11. Comparison of (a) the wave energy flux and (b) wave dissipation rate, observed by the airborne lidar and by in situ wave gauge measurements, with horizontal bars showing the standard deviation of the in situ measurements during the airborne flight time period and vertical bars showing the standard deviation of the running-bin averaging with a window size of 2–4λ, depending on spatial gradients. Legend shows flight numbers (FN), flux locations (W), and locations for dissipation measurements (D_{03}, D_{36}). See Figure 1 for locations W0-W6.

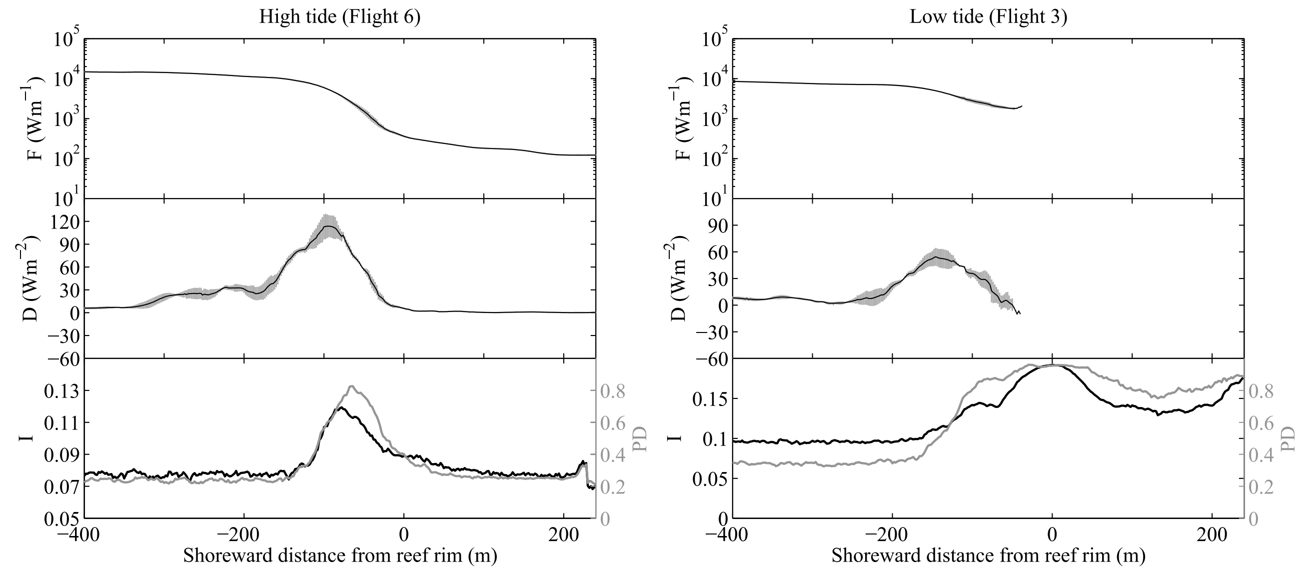

Figure 12. Flight measurements at (left) high and (right) low tides. Spatial profiles of running-bin and ensemble-averaged (a) energy flux, *F*, (b) wave energy dissipation rate, *D*, and (c) cross-swath averaged backscatter intensity (arbitrary units), *I*, and point density, *PD*, measured by the airborne lidar.

flight track. Source terms such as energy input from the wind and energy convergence and divergence due to other processes, including wave refraction, have been neglected in equation (9). Wind input has been neglected based on standard wind input models [*Komen et al.*, 1994; *Romero and Melville*, 2010a] and in situ wind data. The almost unidirectional propagation of the waves at the measurement site is based on the in situ measurements of the wave directional spectrum [*Huang et al.*, 2012] and from the analyzed directional wavenumber spectrum over the reef rim and flat, and in the lagoon, but could also have been based on airborne measurements of the directional properties of the wavefield [cf. *Romero and Melville*, 2010b]. The wave dissipation rates were computed using equation (9) with θ the angle between the along-track direction and the mean wave direction shown by the arrows in Figure 6, and then were bin averaged with a window size of 2–4λ. The use of the mean wave directions in the two regions of Figure 6, rather than the directions of each wave spectral component was dictated by the need for sufficient along track data to resolve wave directional spectra as in Figures 5a and 5d. However, Figure 5d, which is representative of all the data, suggests that the departures of any significant wave energy from the mean directions in those regions is at most $\pm 20°$, which would lead to an error of 6% in equation (9) when using the mean wave direction.

[27] The comparison of wave energy flux and wave energy dissipation rate observed by the airborne lidar and the in situ techniques is presented in Figure 11. The mean value of the standard deviation of airborne lidar measured wave energy flux from the in situ measurements in the lagoon when smoothed by the different window sizes is 8.82 W m^{-1}. The energy flux observed by the airborne lidar also shows a trend of higher values than these of the in situ measurements in the lagoon. However, the wave energy dissipation rate shows better agreement with the in situ measurements. Note that the duration of the lidar surveys is about 32–60 min and the statistics of the wavefield could change within that time. In the figure, the horizontal bars represent the standard deviation of the wave dissipation rate of the in situ measurements during the period of the airborne flight. The results show a satisfactory agreement between the two independent measurements, suggesting that it is feasible to use airborne measurements to observe the wave energy dissipation rates over a coral reef lagoon system.

[28] Figure 12 shows the spatial profiles of the observed average energy flux, the energy dissipation rates, along with lidar backscatter intensity and point density for representative high- tide and low-tide flights. For high tide, the results reveal that the energy flux remains nearly constant at approximately 10^4 W m^{-1} in the ocean, dramatically decreases to O(10^2) W m^{-1} in front of the rim, and decays gradually in the lagoon. The largest dissipation rate occurs in the area between the fore reef and the reef rim due to the occurrence of depth-limited wave breaking [*Huang et al.*, 2012]. The dissipation rate in front of the rim is one to two orders of magnitude larger than that in the lagoon, which is consistent with the in situ observations. The dissipation rate in the ocean is also much smaller than that in front of the rim. Similar results for the energy flux and dissipation rate are observed on the fore reef for the low-tide flights as presented in Figure 12; however, the dissipation rates due to depth-limited breaking are approximately half that of the high-tide data shown here. For high-tide flights, the peak of the cross-swath averaged backscatter intensity and normalized cross-flight point density in front of the rim marks the surf zone due to depth-limited wave breaking. The largest peak of the cross-swath averaged backscatter intensity for the low-tide flights coincides with the exposed rim, and the second peak in front of the rim coincides with the surf zone. Furthermore, at low tide, the backscatter intensity and point density over the lagoon are significantly larger due to scattering from the exposed coral heads.

[29] The results show that the high wave dissipation rates in front of the rim coincide with the high lidar cross-swath averaged backscatter intensity and normalized cross-flight point density. The peak of the backscatter intensity and point density match, or are close to, the peak of the wave dissipation rate. The coincidence of the high values of the lidar backscatter intensity with the high dissipation rate in the surf zone suggests that a statistical quantification of the wave dissipation rate may be investigated using the lidar backscatter intensity or point density.

5. Summary and Conclusions

[30] We used a portable airborne lidar system [*Reineman et al.*, 2009] to measure the wavefield in and around the windward lagoon of Lady Elliot Island in Australia's Great Barrier Reef in April 2008.

[31] The spatial profiles of the measured sea surface displacement were spectrally analyzed using wavelet transform techniques. Measurements show that a large broadening of the dominant wavenumber begins inside the surf zone and throughout the lagoon, which is similar to broadening of typical frequency spectra over reef flats observed in other studies [e.g., *Hardy and Young*, 1996]. Based on the airborne lidar measurements, the wavelet analysis, and linear wave theory, the spatial profiles of the wave energy flux and wave energy dissipation rates over the LEI windward reef and lagoon were computed. It was found that at high tide the wave energy dissipation rate across the fore reef is typically one to two orders of magnitude larger than that in the lagoon, which is consistent with in situ measurements. In particular, the results show that the high lidar backscatter intensity and point density resulting from the high reflectivity of the foam due to depth-limited breaking coincides with the high wave dissipation rates in front of the rim.

[32] *Huang et al.* [2012] demonstrated that the wave energy dissipation is within a factor of order unity of the TKE dissipation in the lagoon. The results presented by this study demonstrate satisfactory agreement between the observation of wave energy flux and wave energy dissipation rates from the airborne scanning lidar measurements and the in situ measurements. This indicates that the wave energy dissipation rates can be effectively and remotely measured from aircraft. From the relationship between the wave dissipation rate and TKE dissipation rate presented by *Huang et al.* [2012], the observations presented in this paper support the conclusion that the TKE dissipation rate in the lagoon can be indirectly estimated by airborne lidar measurements. Such airborne survey techniques present the possibility of studying other reef environments where in situ measurements are not economically feasible. In conjunction with the results of *Baird et al.* [2004], which show nutrient uptake rates to be proportional to the quarter power of the energy dissipation rate, the present results suggest that it may be feasible to use airborne observations to contribute to the identification of potential areas of most rapid nutrient uptake over relatively large areas of coral reefs.

[33] However, measurements of the local water depth are essential for estimating the wave group velocity, wave energy fluxes and the wave dissipation rate. In the absence of an in situ bathymetric survey as used here, the airborne lidar technique could be combined with a bathymetric lidar for simultaneous remote measurements of the water depth and waves over coral reefs. On the other hand, it may be possible to remotely determine the water depth from inversion of airborne measurements of the measured wave phase speed [*Dugan et al.*, 2001]. We have verified (but not shown here) that it is feasible to invert the wave phase speed to obtain the water depth from analyzing the surface wavefields measured by the in situ wave gauge array in this experiment. If the wave phase speed can be measured by airborne imagery techniques, the water depth can be obtained by inversion from the wave phase speed. Preliminary analysis of the images acquired during the present airborne measurements reveal imagery dominated by the bottom features of coral reefs instead of the surface wavefields due to the clarity of the shallow water in the LEI lagoon for much of the experiment; however, that is not to say that such techniques may not be applied with more sophisticated image analysis: a project for the future.

[34] In conclusion, when added to other airborne techniques, including bathymetric lidar, hyperspectral and infrared imaging, the results suggest that it is feasible to contemplate the efficient airborne measurement of physical variables that affect the biogeochemistry and biology of large reef ecosystems like the Great Barrier Reef.

[35] **Acknowledgments.** We thank the Great Barrier Reef Marine Park Authority for granting permits for this research. The support and cooperation of Peter Gash, Wayne Fox, and the staff of both Seair and Lady Elliot Island helped make this project successful. Greg Nippard (UNSW) provided assistance in deploying and maintaining the eddy flux tower in the lagoon. We thank Nick Statom for the manual GPS surveys of the lagoon, Ryan McCabe for bathymetric data surrounding LEI, Ryan Bubinski for the initial data processing, and Leonel Romero for advice and help on various aspects of the data analysis. This research was supported under the Australian Research Council's Discovery Projects funding scheme; project DP0771055 to J.H. Middleton and W.K. Melville, and from internal SIO funding to W.K. Melville. ZCH was partly supported by a fellowship from the Graduate Student Study Abroad Program (NSC97-2917-I-006-119) of the National Science Council of Taiwan.

References

Baird, M. E., M. Roughan, R. W. Brander, J. H. Middleton, and G. J. Nippard (2004), Mass-transfer-limited nitrate uptake on a coral reef flat, Warraber island, Torres Strait, Australia, *Coral Reefs*, *23*(3), 386–396, doi:10.1007/s00338-004-0404-z.

Bretherton, F. P., R. E. Davis, and C. B. Fandry (1976), Technique for objective analysis and design of oceanographic experiments applied to mode-73, *Deep Sea Res.*, *23*(7), 559–582.

Drazen, D., W. K. Melville, and L. Lenain (2008), Inertial scaling of dissipation in unsteady breaking waves, *J. Fluid Mech.*, *611*, 307–332, doi:10.1017/S0022112008002826.

Dugan, J. P., C. C. Piotrowski, and J. Z. Williams (2001), Water depth and surface current retrievals from airborne optical measurements of surface gravity wave dispersion, *J. Geophys. Res.*, *106*(C8), 16,903–16,915, doi:10.1029/2000JC000369.

Emery, W., and R. Thomson (2001), *Data Analysis Methods in Physical Oceanography*, 2nd ed., Elsevier, Amsterdam.

Falter, J. L., M. J. Atkinson, and M. A. Merrifield (2004), Mass-transfer limitation of nutrient uptake by a wave-dominated reef flat community, *Limnol. Oceanogr.*, *49*(5), 1820–1831, doi:10.4319/lo.2004.49.5.1820.

Farge, M. (1992), Wavelet transform and their applications to turbulence, *Annu. Rev. Fluid Mech.*, *24*, 395–458, doi:10.1146/annurev.fl.24.010192.002143.

Gourlay, M. R. (1994), Wave transformation on a coral-reef, *Coastal Eng.*, *23*(1–2), 17–42, doi:10.1016/0378-3839(94)90013-2.

Gourlay, M. R. (1996a), Wave set-up on coral reefs. Part 2. Set-up on reefs with various profiles, *Coastal Eng.*, *28*(1–4), 17–55, doi:10.1016/0378-3839(96)00009-9.

Gourlay, M. R. (1996b), Wave set-up on coral reefs. Part 1. Set-up and wave-generated flow on an idealized two dimensional horizontal reef, *Coastal Eng.*, *27*(3–4), 161–193, doi:10.1016/0378-3839(96)00008-7.

Gourlay, M. R., and G. Colleter (2005), Wave-generated flow on coral reefs—An analysis for two-dimensional horizontal reef-tops with steep faces, *Coastal Eng.*, *52*(4), 353–387, doi:10.1016/j.coastaleng.2004.11.007.

Hardy, T. A., and I. R. Young (1996), Field study of wave attenuation on an offshore coral reef, *J. Geophys. Res.*, *101*(C6), 14,311–14,326, doi:10.1029/96JC00202.

Hearn, C. J., M. J. Atkinson, and J. L. Falter (2001), A physical derivation of nutrient-uptake rates in coral reefs: Effects of roughness and waves, *Coral Reefs*, *20*, 347–356, doi:10.1007/s00338-001-0185-6.

Huang, Z. C., H. H. Hwung, and K. A. Chang (2010), Wavelet based vortical structure detection and length scale estimate for laboratory spilling waves, *Coastal Eng.*, *57*, 795–811, doi:10.1016/j.coastaleng.2010.04.006.

Huang, Z. C., L. Lenain, W. K. Melville, J. H. Middleton, B. D. Reineman, N. Statom, and R. M. McCabe (2012), Dissipation of wave energy and turbulence in a shallow coral reef lagoon, *J. Geophys. Res.*, *117*, C03015, doi:10.1029/2011JC007202.

Jago, O. K., P. S. Kench, and R. W. Brander (2007), Field observations of wave-driven water-level gradients across a coral reef flat, *J. Geophys. Res.*, *112*, C06027, doi:10.1029/2006JC003740.

Komen, G. J., L. Cavaleri, M. Donelan, K. Hasselmann, S. Hasselmann, and P. A. E. M. Janssen (1994), *Dynamics and Modelling of Ocean Waves*, Cambridge Univ. Press, Cambridge, U. K., doi:10.1017/CBO9780511628955.

Longuet-Higgins, M. S., and R. W. Stewart (1964), Radition stress in water waves: A physical discussion, with applications, *Deep Sea Res.*, *11*, 529–562.

Lowe, R. J., J. L. Falter, M. D. Bandet, G. Pawlak, M. J. Atkinson, S. G. Monismith, and J. R. Koseff (2005), Spectral wave dissipation over a barrier reef, *J. Geophys. Res.*, *110*, C04001, doi:10.1029/2004JC002711.

Lowe, R. J., J. L. Falter, S. G. Monismith, and M. J. Atkinson (2009), Wave-driven circulation of a coastal reef-lagoon system, *J. Phys. Oceanogr.*, *39*(4), 873–893, doi:10.1175/2008JPO3958.1.

Lugo-Fernández, A., H. H. Roberts, and J. N. Suhayda (1998), Wave transformations across a Caribbean fringing-barrier Coral Reef, *Cont. Shelf Res.*, *18*(10), 1099–1124, doi:10.1016/S0278-4343(97)00020-4.

Massel, S. R., and M. R. Gourlay (2000), On the modeling of wave breaking and set-up on coral reefs, *Coastal Eng.*, *39*(1), 1–27, doi:10.1016/S0378-3839(99)00052-6.

Monismith, S. G. (2007), Hydrodynamics of coral reefs, *Annu. Rev. Fluid Mech.*, *39*, 37–55, doi:10.1146/annurev.fluid.38.050304.092125.

Nelson, R. C. (1996), Hydraulic roughness of coral reef platforms, *Appl. Ocean Res.*, *18*(5), 265–274, doi:10.1016/S0141-1187(97)00006-0.

Reidenbach, M. A., J. R. Koseff, and M. A. R. Koehl (2009), Hydrodynamic forces on larvae affect their settlement on coral reefs in turbulent, wave-driven flow, *Limnol. Oceanogr.*, *54*(1), 318–330, doi:10.4319/lo.2009.54.1.0318.

Reineman, B. D., L. Lenain, D. Castel, and W. K. Melville (2009), A portable airborne scanning lidar system for ocean and coastal applications, *J. Atmos. Oceanic Technol.*, *26*(12), 2626–2641, doi:10.1175/2009JTECHO703.1.

Romero, L., and W. K. Melville (2010a), Numerical modeling of fetch-limited waves in the Gulf of Tehuantepec, *J. Phys. Oceanogr.*, *40*(3), 466–486, doi:10.1175/2009JPO4128.1.

Romero, L., and W. K. Melville (2010b), Airborne observation of fetch-limited waves in the Gulf of Tehuantepec, *J. Phys. Oceanogr.*, *40*(3), 441–465, doi:10.1175/2009JPO4127.1.

Stein, M. L. (1999), *Statistical Interpolation of Spatial Data: Some Theory for Kriging*, Springer, New York.

Symonds, G., K. P. Black, and I. R. Young (1995), Wave-driven flow over shallow reefs, *J. Geophys. Res.*, *100*(C2), 2639–2648, doi:10.1029/94JC02736.

Tennekes, L., and J. L. Lumley (1972), *A First Course in Turbulence*, MIT Press, Cambridge, Mass.

Walsh, E. J., D. W. Hancock, D. E. Hines, R. N. Swift, and J. F. Scott (1985), Directional wave spectra measured with the surface contour radar, *J. Phys. Oceanogr.*, *15*(5), 566–592, doi:10.1175/1520-0485(1985)015<0566:DWSMWT>2.0.CO;2.

Young, I. R. (1989), Wave transformation over coral reefs, *J. Geophys. Res.*, *94*(C7), 9779–9789, doi:10.1029/JC094iC07p09779.

Z.-C. Huang, Graduate Institute of Hydrological and Oceanic Sciences, National Central University, Taoyuan 32001, Taiwan.

L. Lenain, W. K. Melville, and B. D. Reineman, Scripps Institution of Oceanography, University of California, San Diego, La Jolla, CA 92093-0213, USA. (kmelville@ucsd.edu)

J. H. Middleton, School of Aviation, University of New South Wales, Sydney, NSW 2052, Australia.